ADVANCED FUNCTIONAL MATERIALS
www.afm-journal.de

Binary Ferromagnetic Nanostructures: Fabrication, Static and Dynamic Properties

*Junjia Ding and Adekunle O. Adeyeye**

The fabrication of large area binary magnetic nanostructures made from one or two ferromagnetic materials (Ni and $Ni_{80}Fe_{20}$) is reported using self-aligned shadow deposition technique. The static and dynamic properties are characterized using magneto-optical Kerr effects (MOKE) and broadband ferromagnetic resonance spectroscopy. Compared with $Ni_{80}Fe_{20}$ nanomagnets made using a conventional lithographic technique from identical resist templates, tunable magnetization switching is observed with a marked increase in the coercive field and more adjustable dynamic response for the $Ni_{80}Fe_{20}/Ni_{80}Fe_{20}$ and $Ni/Ni_{80}Fe_{20}$ binary structures. The results are validated by direct domain imaging using magnetic force microscopy and micromagnetic simulations.

1. Introduction

Artificial ferromagnetic nanostructures with periodic lateral contrast in magnetization are known as "magnonic crystals" (MCs), conceived as the magnetic analogue of photonic crystals.[1–3] Recently, there is a growing interest in the fundamental understanding of the spin wave propagation in MCs because of their potential use in a wide range of applications such as microwave resonators, filters,[4] and spin wave logic devices.[5] The band spectrum of MCs consists of allowed states (magnonic bands) and forbidden states (magnonic gaps) that can be tuned by magnetic fields and geometrical parameters.[1–3] With advances in controlled nanofabrication techniques, it is now possible to synthesize high-quality magnetic nanostructures with precisely controlled dimensions.

A number of periodic structures have been identified as candidates for MCs including 1D magnetostatically coupled nanowires (NW),[6,7] periodically modulated YIG films[8] and 2D ferromagnetic antidot nanostructures.[9–11] Recently, band gap tunability has been demonstrated in synthetic bicomponent MCs consisting of alternating $Ni_{80}Fe_{20}$ NWs in direct contact with Co NWs[12] and 2D antidot structures in which the holes are filled with another ferromagnetic material.[13]

To fully exploit MCs in applications, however, the key challenge associated with the nanofabrication of tunable bicomponents magnonic crystals consisting of two contrasting ferromagnetic materials must be resolved. There are various limitations with the quality of MCs produced with the multilevel electron beam lithographic approach described in ref. [12] including the issue of alignment of the two contrasting NWs.

In this article, we describe a "self-aligned shadow deposition" technique for synthesizing novel large area MCs consisting of one or two contrasting ($Ni_{80}Fe_{20}/Ni_{80}Fe_{20}$ and $Ni/Ni_{80}Fe_{20}$) ferromagnetic materials (FMs). The key advantage of this nanofabrication process is that, unlike the multilevel electron beam lithographic process, no alignment between the two FM layers is required (i.e., self-alignment). In addition, the deposition of the two materials can be performed without breaking the vacuum in the same process step. Using a combination of deep ultraviolet lithography (DUV) resist templates and a self-aligned shadow deposition method, we have prepared arrays of binary ferromagnetic nanostructures over large areas. High aspect ratio resists templates were first prepared by DUV lithographic technique as described in ref. [14]. This was followed by the electron beam deposition of Ni and $Ni_{80}Fe_{20}$ materials at varied deposition angles and subsequent lift-off process. For a controlled experiment, $Ni_{80}Fe_{20}$ nanostructures were also fabricated from the same resist templates using conventional deposition technique. The collective magnetization reversal processes of the nanostructures at room temperature were characterized by the magneto-optical Kerr effect (MOKE) with a 50-μm laser spot size. The reflected laser beam from the sample surface is polarization analyzed in order to access the longitudinal Kerr effect, which is sensitive to the component of magnetization lying in the optical plane of incidence.[15] An electromagnet allows magnetic fields to be applied in the plane of the sample in order to measure a full hystersis loop. We characterized their dynamic properties using broadband ferromagnetic resonance spectroscopy (FMR) in the frequency range from 10 MHz to 20 GHz.

We observed tunable magnetization switching process on the $Ni_{80}Fe_{20}/Ni_{80}Fe_{20}$ and $Ni/Ni_{80}Fe_{20}$ binary structures with marked increase in the coercive field when compared with the $Ni_{80}Fe_{20}$ nanostructures. We further characterized the magnetization reversal mechanism by directly imaging the magnetization states at various magnetic field histories using magnetic force microscopy. Our experimental results are in very good agreement with micromagnetic simulations.

J. Ding, Prof. A. O. Adeyeye
Information Storage Materials Laboratory
Department of Electrical and Computer Engineering
National University of Singapore
117576, Singapore
E-mail: eleaao@nus.edu.sg

DOI: 10.1002/adfm.201201432

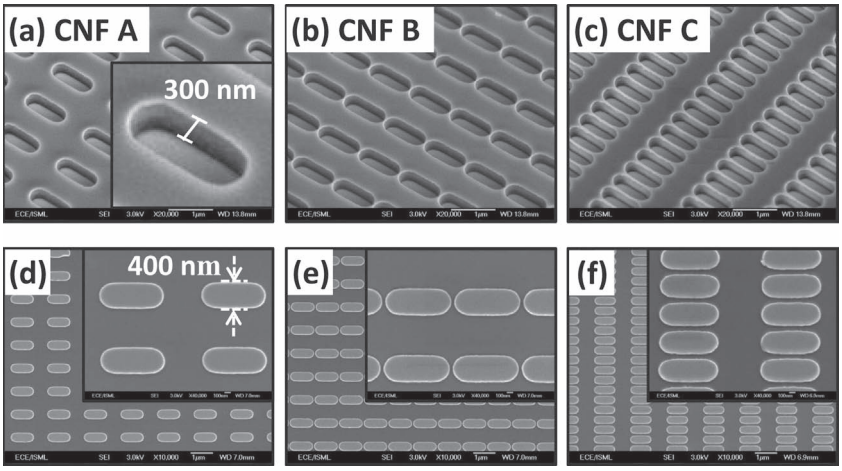

Figure 1. Scanning electron micrographs of the surface profile of the patterned resist of an array of ellipsoidal nanostructures: a) configuration A, b) configuration B, and c) configuration C. d–f) $Ni_{80}Fe_{20}$ nanostructures fabricated by using normal electron beam evaporation with corresponding resist pattern.

2. Results and Discussion

2.1. Fabrication

Periodic arrays of ellipsoidal patterns were defined in a 240-nm thick DUV resist on top of a 60-nm bottom antireflection coating on silicon substrates. Details of the resist template fabrication process are described elsewhere.[14] Here, we focus on the process involved in creating binary magnetic nanostructures from patterned resist templates. To demonstrate this nanofabrication technique, we have focused on three resist patterns, namely: configuration A ("CNF A") consisting of isolated ellipse resist patterns; configuration B ("CNF B") consisting of ellipse resist pattern with the elements coupled along the long axis of the ellipse and for configuration C ("CNF C"), the elements of the resist pattern are coupled along the short axis of the ellipse. In order to verify the profile of the resist patterns using a scanning electron microscope (SEM), a 5-nm Au metal layer was deposited to prevent resist charging effect. Shown in **Figure 1**a–c are the resist profiles corresponding to the three configurations CNF A, CNF B and CNF C, respectively. The SEM images show uniform resist profiles with well-defined sidewalls. To create magnetic nanostructures from the resist patterns, a 20-nm-thick $Ni_{80}Fe_{20}$ layer was deposited on all the three lattice configurations using electron beam evaporation at a rate of 0.2 Å/s in a chamber with a base pressure of 4×10^{-8} Torr, followed by the deposition of 5-nm-thick Ti capping layer. Shown in Figure 1d–f are the corresponding SEM images of the resulting $Ni_{80}Fe_{20}$ nanostructures for the three configurations. The inter-element spacing for CNF B and CNF C is kept at around 100 nm. The SEM images show well-defined magnetic elements with good dimensionality control.

To create $Ni_{80}Fe_{20}/Ni_{80}Fe_{20}$ and $Ni/Ni_{80}Fe_{20}$ binary structures from the identical resist templates shown in Figure 1a–c, a tilt-table sample holder was specially designed and used in the shadow deposition process using the same electron beam deposition chamber. The underlying principle is similar to conventional shadow deposition, in which a pattern is created when a shadow mask or stencil is placed between the source of evaporated material and the substrate.[16] Previously, the shadow deposition method combined with angle deposition process was used to fabricate sub-micrometer-scale thin-film structures and simple multilevel structures by single-mask lift-off processing.[17] In our approach, the thick resist sidewalls of the patterns play the role as the stencil in conventional shadow deposition. Schematic illustrations of the fabrication steps of $Ni/Ni_{80}Fe_{20}$ binary structures are shown in **Figure 2**a–c. A shadow area is formed on the left hand side of the pattern when the material is deposited from right of the sample, while the shadow area appears on the right hand side of the patterns when the deposition is performed from the left of the sample. The shadow patterns from the two deposition processes are self-aligned by the uniform resist and precise control of deposition angle. The size of the shadow area can be controlled conveniently by adjusting the deposition angle. In order to ensure that the two shadow deposition processes result in geometrically identical patterns, we performed our depositions with the substrate tilted at ±35° away from the normal direction of the sample. To create $Ni/Ni_{80}Fe_{20}$ binary structures, the Ni (FM1) and $Ni_{80}Fe_{20}$ (FM2) materials were deposited on the right and left of the pattern sequentially, followed by the lift-off process. $Ni/Ni_{80}Fe_{20}$ binary structures with identical lateral dimension separated by a small gap can be seen in the enlarged SEM images (insets of Figure 2d–f). The detailed SEM images of Figure 2d,e showing a small gap between the two subelements of the binary are shown in Figure 2g,h, respectively. By adjusting the deposition angle, it is possible to control the region of overlap as shown in Figure 2i,j for deposition performed at ±23° from the same resist templates. In order to demonstrate the versatility of this process, we have used nanowire (NW) resist templates to create binary NWs from two different materials as shown in **Figure 3**. Shown in Figure 3a–c are the schematics of the normal NWs, binary NWs, and thickness modulated NWs structures we have fabricated, respectively. The corresponding SEM micrographs of the NW structures are shown in Figure 3d–f. The thickness modulated NWs were fabricated using a two-stage deposition process. In the first deposition stage, the sample was not titled, while in the second deposition stage, the sample was titled at ±23°. Thus, we have shown that complex structures can be fabricated using this approach. This method is compatible with other resist template created from different lithographic techniques.

In the following section, we will focus on the static and dynamic behavior of $Ni_{80}Fe_{20}/Ni_{80}Fe_{20}$ and $Ni/Ni_{80}Fe_{20}$ binary structures, using conventional $Ni_{80}Fe_{20}$ nanostructures fabricated from the same templates as a reference.

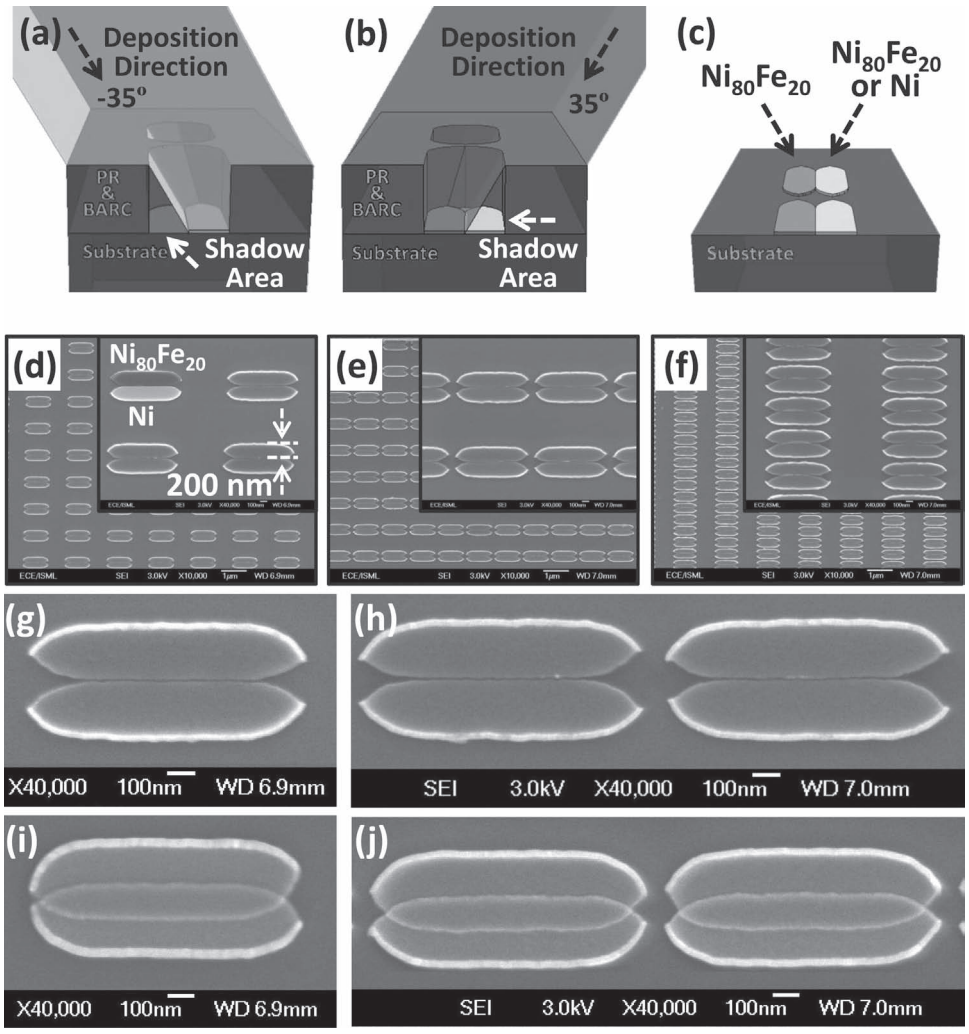

Figure 2. a,b) Schematics of the self-aligned shadow deposition method. c) Sketch of the final binary structure. Scanning electron micrographs of the d) isolated Ni/$Ni_{80}Fe_{20}$ binary structures and magnetically coupled Ni/$Ni_{80}Fe_{20}$ binary structures with e) CNF B and f) CNF C. The magnified SEM images of (d) and (e) are shown in (g) and (h), respectively. Binary nanostructure with large overlay area for CNF A and CNF B are shown in (i) and (j), respectively.

2.2. Static Magnetic Properties

Figure 4a shows the normalized MOKE loop from $Ni_{80}Fe_{20}$ nanostructures with CNF A. To determine the switching process, the differential of the MOKE loop as a function of the applied field from the negative to positive saturation field is also plotted. The two peaks observed correspond to the different switching processes occurring as the applied magnetic field is swept. In this case, the peak corresponds to the nucleation (70 Oe) and annihilation (145 Oe) of the vortex core, respectively. The reversal mechanism agrees with previous results.[18,19]

Shown in Figure 4b is the MOKE loop and the corresponding differential curve for the $Ni_{80}Fe_{20}/Ni_{80}Fe_{20}$ binary structures. Compared with Figure 4a, there is a significant increase in the coercive field from 70 to 220 Oe due to the strong shape anisotropy resulting from the splitting of the $Ni_{80}Fe_{20}$ nanostructures in Figure 4a into two identical $Ni_{80}Fe_{20}/Ni_{80}Fe_{20}$ nanostructures by the shadow deposition process. The higher length-width ratio (1:5) makes it easier for the $Ni_{80}Fe_{20}/Ni_{80}Fe_{20}$ structures to adopt single domain states at remanence for field along the major axis.

In Figure 4c, the MOKE loop and the differential curve for the Ni/$Ni_{80}Fe_{20}$ binary nanostructures display a two-step switching process corresponding to the distinct reversal of the Ni nanostructures at low field (150 Oe) and $Ni_{80}Fe_{20}$ nanostructures at high field (290 Oe). A region of antiparallel relative alignment of magnetization is clearly seen. This is not observed in Figure 4a,b. These results demonstrate that the magnetic behavior of binary magnetic nanostructures can be systematically tuned using the same resist templates.

Interestingly, due to the strong magnetostatic coupling between Ni and $Ni_{80}Fe_{20}$ elements in the binary structures, the switching field of the $Ni_{80}Fe_{20}$ elements in the Ni/$Ni_{80}Fe_{20}$ structures is higher than that in the $Ni_{80}Fe_{20}/Ni_{80}Fe_{20}$ structures. The total energy of the Ni/$Ni_{80}Fe_{20}$ binary structures is minimized when the two adjacent elements are magnetized antiparallel

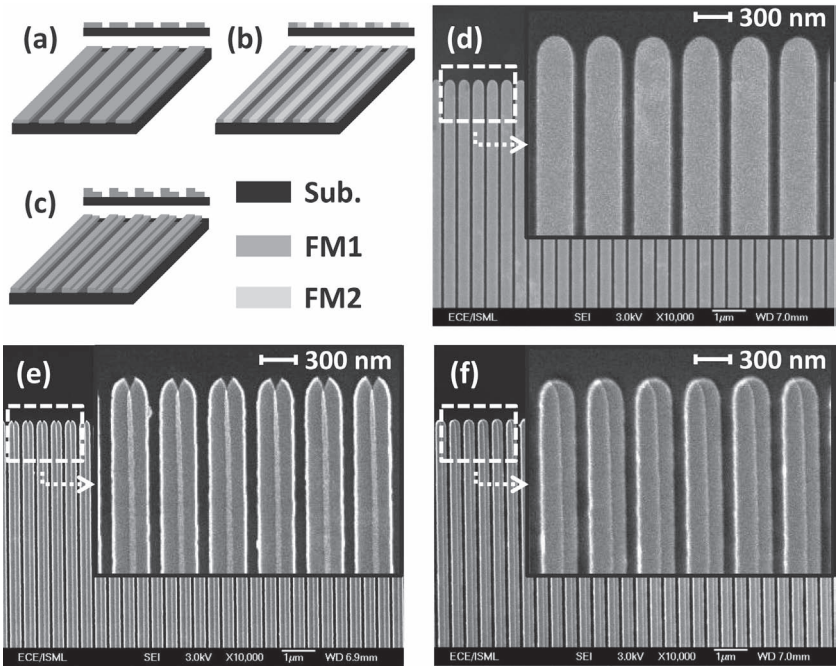

Figure 3. Schematic illustration of the a) normal NWs, b) binary NWs, and c) thickness modulated NWs. The corresponding SEM micrographs of the NW structures are shown in (d–f), respectively.

relative to each other.[20] This suggests that introducing two kinds of material with varied magnetic contrasts can be used to further control the magnetic switching processes.

In order to validate the reversal mechanism, we have directly imaged the magnetic states of the nanostructures described in Figure 4a–c using magnetic force microscopy (MFM) in the phase detection mode with a commercial CoCr coated Si cantilever tips magnetized along the tip axis. The scan height was maintained at 70 nm for all the measurements. Shown in Figure 4d is the MFM image (corresponding to position α on the M-H loop in Figure 4a) for the $Ni_{80}Fe_{20}$ structures, after first saturating the sample in a field of –1500 Oe and then reducing the field back to zero. The MFM image shows that the $Ni_{80}Fe_{20}$ nanostructures have adopted various types of metastable magnetic states, in agreement with previous report by Jain et al.[18]

For direct comparison, we have also imaged the magnetization states of the binary structures. Shown in Figure 4e is the MFM image for $Ni_{80}Fe_{20}/Ni_{80}Fe_{20}$ binary structures (corresponding to position β on the M-H loop in Figure 4b). The image reveals that the $Ni_{80}Fe_{20}/Ni_{80}Fe_{20}$ structures are in single domain states. This is in agreement with the M-H loop in Figure 4b where full magnetization is obtained at zero field after first saturating the structures. The MFM image for the $Ni/Ni_{80}Fe_{20}$ binary structures (corresponding at position γ on the M-H loop in Figure 4c) is shown in Figure 4f. As expected, the result is similar to the magnetization state obtained on the $Ni_{80}Fe_{20}/Ni_{80}Fe_{20}$ binary structures shown Figure 4e.

To validate the antiparallel relative alignment of magnetization observed in the M-H loop shown Figure 4d, a large magnetic field of –1500 Oe was first applied along the long axis after which the field was subsequently increased to 250 Oe above the switching field of the Ni elements in the binary structures. Shown in Figure 4g is the MFM image taken at remanence (corresponding to position δ on the M-H loop in Figure 4c). The contrast differences at the two ends of each $Ni/Ni_{80}Fe_{20}$ structures clearly show that the magnetizations of the $Ni/Ni_{80}Fe_{20}$ binary structures are aligned antiparallel relative to each other in agreement with the M-H loop.

To further investigate the magnetization reversal mechanism, we performed systematic micromagnetic modeling using LLG Micromagnetics Simulator.[21] Standard parameters for $Ni_{80}Fe_{20}$ (gyromagnetic ratio $\gamma = 2.8$ GHz/kOe, saturation magnetization $M_s = 800$ emu·cm^{-3}, exchange constant $A = 1.05 \times 10^{-6}$ erg·cm^{-1}, and anisotropy constant $K_U = 0$) and Ni ($M_s = 490$ emu·cm^{-3}, $A = 0.9 \times 10^{-6}$ erg·cm^{-1} and $K_U = 0$) were used in the simulation. The masks used in the simulations were derived from the SEM micrographs with a cell size of 5 nm × 5 nm × 20 nm in the simulations. We simulated individual $Ni_{80}Fe_{20}$, $Ni_{80}Fe_{20}/Ni_{80}Fe_{20}$ and $Ni/Ni_{80}Fe_{20}$ structures by assuming that the elements in the array are magnetically isolated (CNF A).

Shown in **Figure 5**a–c are the simulated M-H loops corresponding to the experimental results shown in Figure 4a–c, respectively. The simulated results reproduced most of the features of experimentally observed switching processes. The trend in the coercive field is also in qualitative agreement with experimental results. In addition, the simulated M-H loop of $Ni/Ni_{80}Fe_{20}$ binary structure displays a clear two-step switching process (Figure 4c) in agreement with the experimental results. The small differences in the switching field values may be attributed to the fact that the simulation is performed on individual elements while the collective reversal of the ensemble was measured. It is therefore difficult to replicate the exact roughness and inhomogeneity across the entire arrays in the simulation.

The magnetization states corresponding to the various positions on the simulated M-H loops in Figure 5a–c for $Ni_{80}Fe_{20}$, $Ni_{80}Fe_{20}/Ni_{80}Fe_{20}$ and $Ni/Ni_{80}Fe_{20}$ nanostructures are shown in Figure 5d–f. As shown in Figure 5d(i), due to the shape anisotropy, some weak domain walls are formed at the left and right end of the $Ni_{80}Fe_{20}$ nanostructure at remanence for the $Ni_{80}Fe_{20}$ nanostructure. A metastable vortex state is observed when a reverse field of 100 Oe is applied as shown in Figure 5d(ii). The $Ni_{80}Fe_{20}$ nanostructure is fully saturated when the reverse field is increased to 450 Oe as shown in Figure 5d(iii). The corresponding simulated magnetization states for the $Ni_{80}Fe_{20}/Ni_{80}Fe_{20}$ and $Ni/Ni_{80}Fe_{20}$ binary structures are shown in Figure 5e and f, respectively. As shown in Figure 5e(i) and Figure 5f(i), when the applied field is reduced from positive or negative saturation to zero, both of the $Ni_{80}Fe_{20}/Ni_{80}Fe_{20}$ and $Ni/Ni_{80}Fe_{20}$ binary structures adopted single domain states along applied field direction due to the strong shape anisotropy.

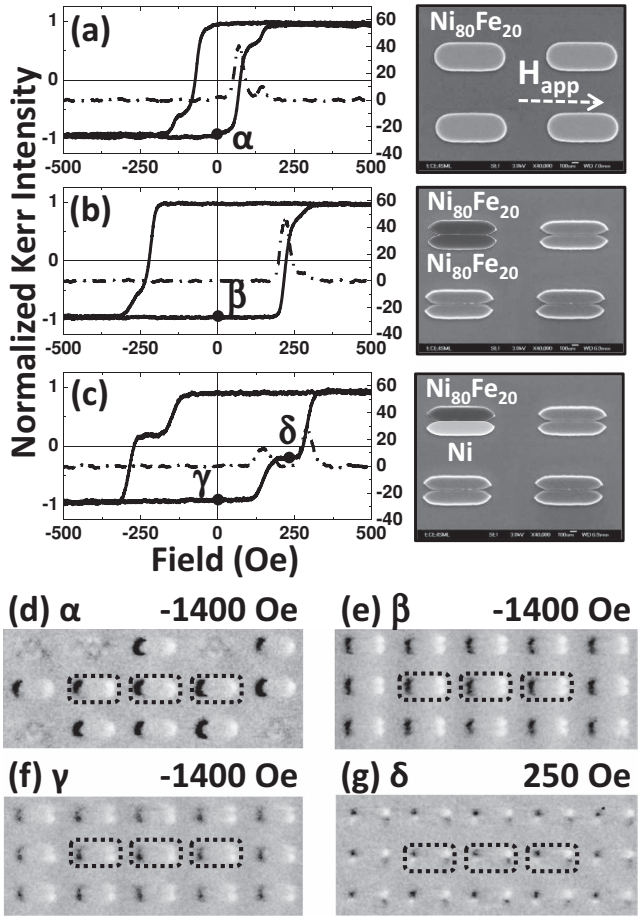

Figure 4. Hysteresis loops of a) $Ni_{80}Fe_{20}$ nanostructures, b) $Ni_{80}Fe_{20}$/$Ni_{80}Fe_{20}$ binary structures, and c) Ni/$Ni_{80}Fe_{20}$ binary structures. d–f) The remnant magnetic states observed using MFM for the three structures are shown in, respectively. g) MFM image of the Ni/$Ni_{80}Fe_{20}$ binary structure for H_{max} = 250 Oe at remanence.

However, when a reverse field of 300 Oe is applied, a distinct difference between the magnetization states for $Ni_{80}Fe_{20}$/$Ni_{80}Fe_{20}$ and Ni/$Ni_{80}Fe_{20}$ binary structures can be observed, as shown in Figure 5e(ii) and Figure 5f(ii), respectively. One of the two $Ni_{80}Fe_{20}$ subelements in the $Ni_{80}Fe_{20}$/$Ni_{80}Fe_{20}$ binary structure is fully switched at lower reversal field as shown in Figure 5e(ii). Simultaneously, the other $Ni_{80}Fe_{20}$ subelement forms a metastable state in which a vortex core is nucleating at the left corner of the structure. This state persists for a field range of about 30 Oe due to the effect of dipolar interaction between the two subelements, which favors the antiparallel orientation of the magnetization of the two adjoining subelements.[22] The switching sequence for these two subelements may be affected by the presence of defects and roughness. This metastable state was not observed in the experimental MOKE loop in Figure 4b probably due to the switching distribution of a number of isolated structures on the sample. A clear antiparallel relative alignment of magnetization is observed for Ni/$Ni_{80}Fe_{20}$ binary structures (Figure 5f(ii)), in agreement with the MFM image shown in Figure 4g. It verifies that the Ni subelements switches at a lower reverse field which results in a stable antiparallel relative alignment of magnetization ground state due to the presence of the dipolar interaction between the two subelements.

In order to understand the role of dipolar coupling between the two subelements in the binary nanostructure, we performed several micromagnetic simulations, as shown in Figure 5g, including simulation on isolated Ni subelement, isolated $Ni_{80}Fe_{20}$ subelement, Ni/$Ni_{80}Fe_{20}$ nanostructure with a gap size (g) varied from 5 nm to 100 nm. We found that all the binary structures displayed two-step magnetization switching. However, the field region where the two subelements are in antiparallel relative alignment of magnetization is strongly dependent on the dipolar coupling (for g = 5 nm, ΔH_s = 210 Oe; for g = 50 nm, ΔH_s = 160 Oe, and for g = 100 nm, ΔH_s = 140 Oe). This clearly shows that the strength of dipolar coupling can be controlled by varying the gap size.

2.3. Effects of Magnetostatic Coupling

We further investigate the effects of coupling neighboring elements by comparing the reversal process of magnetically coupled $Ni_{80}Fe_{20}$, $Ni_{80}Fe_{20}$/$Ni_{80}Fe_{20}$ and Ni/$Ni_{80}Fe_{20}$ structures arranged in configurations CNF B and CNF C with configuration CNF A. Shown in **Figure 6**a are the M-H loops for magnetically coupled $Ni_{80}Fe_{20}$, $Ni_{80}Fe_{20}$/$Ni_{80}Fe_{20}$ and Ni/$Ni_{80}Fe_{20}$ structures for fields applied along the major axis (CNF B). For the coupled $Ni_{80}Fe_{20}$ nanostructures, the magnetization reversal process is characterized by a sharp switching with a coercive field of 115 Oe. This is markedly different from the hysteresis loop for isolated $Ni_{80}Fe_{20}$ nanostructures shown in Figure 4a suggesting that there is a strong configurational anisotropy introduced by the linear chain arrangement.[18] As expected, there is also a significant difference in the reversal mechanism between magnetically coupled $Ni_{80}Fe_{20}$ and binary ($Ni_{80}Fe_{20}$/$Ni_{80}Fe_{20}$ and Ni/$Ni_{80}Fe_{20}$) structures. However, compared with Figure 4b,c, the reversal mechanism of the coupled $Ni_{80}Fe_{20}$/$Ni_{80}Fe_{20}$ and Ni/$Ni_{80}Fe_{20}$ is not significantly different from the isolated structures except for the slight increase in the coercive fields.

Shown in Figure 6b are the representative MOKE loops when the nanostructures are magnetically coupled along the minor axis (CNF C). Compared with Figure 6a, the shapes of the M-H loops are shared presumably due to the direct competition between shape and configurational anisotropies. Interestingly, the magnetic behavior of the $Ni_{80}Fe_{20}$/$Ni_{80}Fe_{20}$ and Ni/$Ni_{80}Fe_{20}$ binary structures are markedly different when compared with Figure 4a–c. The switching field of $Ni_{80}Fe_{20}$/$Ni_{80}Fe_{20}$ binary structures is close to that of $Ni_{80}Fe_{20}$ in the Ni/$Ni_{80}Fe_{20}$ structures when the elements are coupled along the major axis (Figure 6a). However, when the elements are coupled along the minor axis, the switching field of $Ni_{80}Fe_{20}$/$Ni_{80}Fe_{20}$ binary structures is much lower than that of $Ni_{80}Fe_{20}$ in the Ni/$Ni_{80}Fe_{20}$ binary structures. This can be also attributed to the competition between configurational anisotropy and dipolar coupling between elements. The results in Figure 6a suggest the magnetization reversal process is dominated by

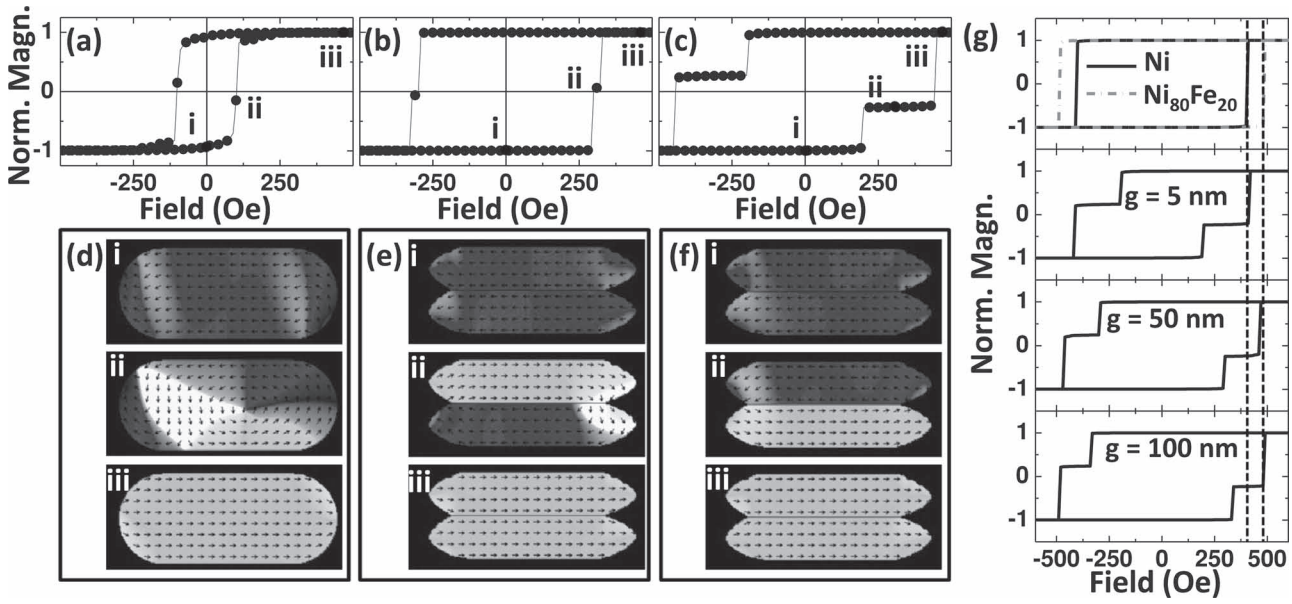

Figure 5. Simulated hysteresis loops for the individual a) $Ni_{80}Fe_{20}$ nanostructure, b) $Ni_{80}Fe_{20}/Ni_{80}Fe_{20}$ binary structure, and c) $Ni/Ni_{80}Fe_{20}$ binary structure. d–f) The simulated magnetization states corresponding to positions (i–iii) on the M-H for the three structures, respectively. g) Simulated M-H loop for isolated Ni subelement, isolated $Ni_{80}Fe_{20}$ subelement, and $Ni/Ni_{80}Fe_{20}$ nanostructure as a function of a gap size, *g*.

configurational anisotropy along the major axis. The reversal process of the linear chain arrangement resembles that of magnetic NWs for fields applied along the wire easy axis. For configuration CNF C (Figure 6b), however, the magnetostatic coupling between the Ni and $Ni_{80}Fe_{20}$ subelements is much stronger and dominates the reversal process. In this case, the magnetostatic coupling between the switched Ni subelements and unswitched $Ni_{80}Fe_{20}$ subelements will push the switching of the $Ni_{80}Fe_{20}$ subelements to a higher H_{app} in $Ni/Ni_{80}Fe_{20}$ structure.

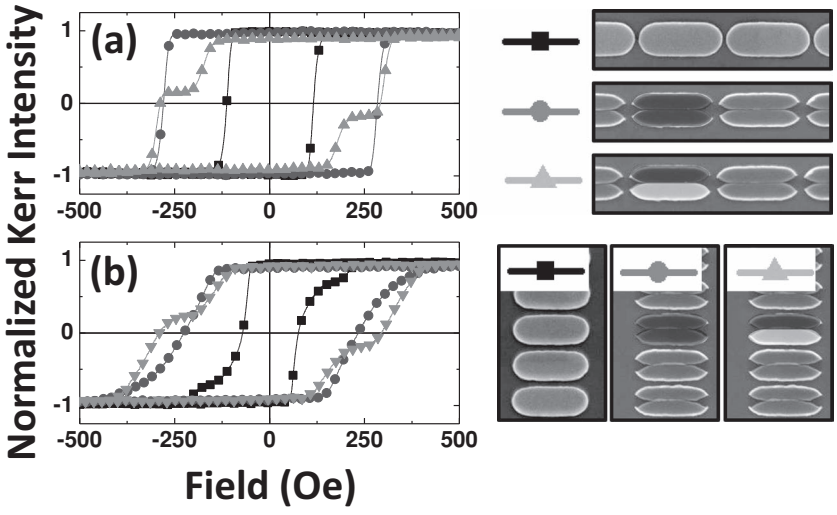

Figure 6. A comparison of the M-H loops for $Ni_{80}Fe_{20}$ nanostructure, $Ni_{80}Fe_{20}/Ni_{80}Fe_{20}$ and $Ni/Ni_{80}Fe_{20}$ binary nanostructures for configurations a) CNF B and b) CNF C when the field is applied along the ellipse major axis.

2.4. Dynamic Properties

The dynamic properties of $Ni_{80}Fe_{20}$, $Ni_{80}Fe_{20}/Ni_{80}Fe_{20}$ and $Ni/Ni_{80}Fe_{20}$ binary structures were probed using FMR. Coplanar waveguide (CPW) with signal line width of 20 μm were fabricated on top of the magnetic nanostructures using conventional optical lithography, metallization of Al_2O_3(50 nm)/Au(150 nm) followed by a lift-off process. A schematic of our FMR measurements setup is described in ref. [23]. The two ports of a microwave vector network-analyzer (VNA) were connected to the CPW using G-S-G-type microwave probes. For a fixed applied field, the FMR measurement was performed by sweeping the frequency (H_{app}) in the range from 1 to 20 GHz. This process was repeated for various H_{app} values starting from negative saturation field (–1500 Oe), passing through zero, and then gradually increasing to positive saturation field (1500 Oe). The H_{app} is applied along the major axis of the patterns, while the microwave magnetic field produced by the signal line of CPWs is applied along the minor axis. **Figure 7**a–c show representative absorption curves as a function of static magnetic field strength for isolated $Ni_{80}Fe_{20}$, $Ni_{80}Fe_{20}/Ni_{80}Fe_{20}$ and $Ni/Ni_{80}Fe_{20}$ binary structures (CNF A), respectively. As expected, for all the structures, the resonance frequencies shift to lower range as the magnitude of H_{app} is decreased. For the $Ni_{80}Fe_{20}$ nanostructures, only one resonance peak is observed in agreement with our previous results.[24] The $Ni_{80}Fe_{20}/Ni_{80}Fe_{20}$ binary structures have

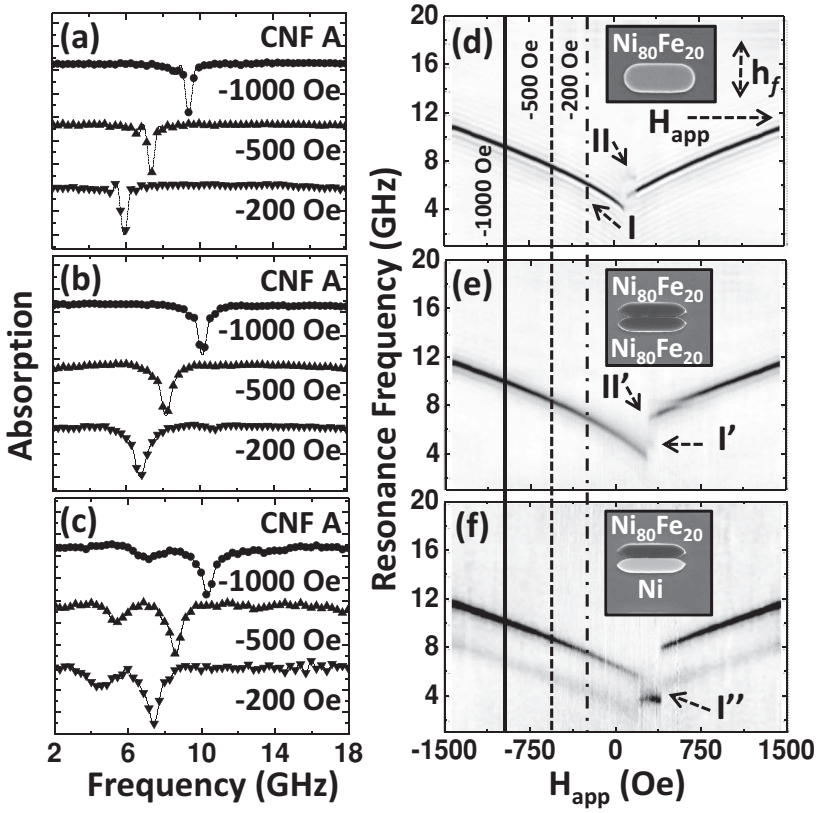

Figure 7. Representative FMR absorption traces of isolated a) $Ni_{80}Fe_{20}$ nanostructures, b) $Ni_{80}Fe_{20}/Ni_{80}Fe_{20}$ binary nanostructures and c) $Ni/Ni_{80}Fe_{20}$ binary nanostructures for varying H_{app} values. d–f) The corresponding 2D absorption spectra for the three structures, respectively.

higher resonance frequencies compared with the $Ni_{80}Fe_{20}$ structures for the same static magnetic field due to the strong shape anisotropy. The aspect ratio of the $Ni_{80}Fe_{20}$ elements in the $Ni_{80}Fe_{20}/Ni_{80}Fe_{20}$ binary structures is twice of that for $Ni_{80}Fe_{20}$ nanostructures. This increases the demagnetizing factor along the minor axis, while decreases along the major axis. The magnetostatic coupling between the $Ni_{80}Fe_{20}$ elements for in the $Ni_{80}Fe_{20}/Ni_{80}Fe_{20}$ binary structures also modifies the demagnetizing factor of the structures. The high frequency resonance peaks of the $Ni_{80}Fe_{20}/Ni_{80}Fe_{20}$ binary structures compared to the $Ni_{80}Fe_{20}$ structures can be explained using Kittel's equation.[25] For the $Ni/Ni_{80}Fe_{20}$ binary structures, two distinct absorption peaks are clearly identified as a function of applied field. These two modes could be the acoustic (lower frequency peak) and optical (higher frequency peak) modes of the binary structures. One can also infer that the higher frequency mode mainly originates from $Ni_{80}Fe_{20}$ subelements, while the lower frequency mode is mostly localized in the Ni subelements due to the lower saturated magnetization of Ni (490 emu·cm^{-3}) compared to that of $Ni_{80}Fe_{20}$ (800 emu·cm^{-3}) based on the Kittel's equation for saturated state. Similar phenomenon has also been observed for NWs with both identical and different width.[26] We also found that the resonance frequencies of $Ni_{80}Fe_{20}$ in the $Ni/Ni_{80}Fe_{20}$ binary structures is higher than that in the $Ni_{80}Fe_{20}/Ni_{80}Fe_{20}$ binary structures for all H_{app} values due to the weaker magnetostatic coupling between the Ni and $Ni_{80}Fe_{20}$ subelements, which reduces the internal field along the major axis of the nanomagnets.[27]

Shown in Figure 7d–f are the full hysteresis loops FMR absorption spectra for $Ni_{80}Fe_{20}$, $Ni_{80}Fe_{20}/Ni_{80}Fe_{20}$ and $Ni/Ni_{80}Fe_{20}$ structures, respectively. These data correspond to the forward half of a full loop (i.e., the applied field was gradually increased from –1500 to +1500 Oe). The absorption intensities are represented in gray scale for each frequency and H_{app} values. The bright region indicates low microwave absorption, while the dark region represents strong absorption for the corresponding H_{app} and frequency values. The FMR results are in very good agreement with the M-H loops shown in Figure 4a–c. While the $Ni_{80}Fe_{20}$ and $Ni_{80}Fe_{20}/Ni_{80}Fe_{20}$ structures display single resonance frequency as a function of applied field, the $Ni/Ni_{80}Fe_{20}$ binary structures show two distinct frequencies corresponding to the mode from Ni elements at low frequency and $Ni_{80}Fe_{20}$ elements at high frequency.

The different switching processes for the three structures discussed in Section 2.3 will also influenced the dynamic response in the transition field regime. Two weak modes (mode I and II) appears in $Ni_{80}Fe_{20}$ structure in the transition field range (from 90 to 150 Oe) as shown in Figure 7d. One possible origin of the multiple modes observed in this field range may be due to the various radial and azimuthal modes of the chiral spin magnetization around the vortex core.[28] Another possible reason may be due to the fact that the switched part, which occupied most of the area of the $Ni_{80}Fe_{20}$ structures, is the origin of mode I, while mode II is localized in the unswitched part of the $Ni_{80}Fe_{20}$ structures. Similarly, two modes are observed in $Ni_{80}Fe_{20}/Ni_{80}Fe_{20}$ structures for field range from 280 to 320 Oe, as shown in Figure 7e. In this case, the intensity of the lower frequency mode, I′, is much weaker than the higher frequency mode, II′. This suggests that mode II′ originates from the fully switched $Ni_{80}Fe_{20}/Ni_{80}Fe_{20}$ structures, while the frequency of mode I′ is lower due to the fact that antiparallel relative alignment of magnetization is formed in some of the $Ni_{80}Fe_{20}/Ni_{80}Fe_{20}$ structures.[26] The weaker intensity of mode I′ shows that only few $Ni_{80}Fe_{20}/Ni_{80}Fe_{20}$ structures formed antiparallel relative alignment of magnetization in the whole array. A discontinuous mode observed at around 540 Oe may be due to the fact that the area around the corner and edge of the structure is hard to be saturated in the field range. For $Ni/Ni_{80}Fe_{20}$ binary structures, only one mode, I″, can be observed in the transition field range (≈190–350 Oe), as shown in Figure 7f. Similar results were observed in an alternating width NW array with antiparallel magnetization ground state.[27] The almost field-independent slope of the this mode (I″) suggests the formation of acoustic and optical modes in the binary structures with antiparallel

alignment magnetization ground state. The optical mode (higher-frequency one) is not visible in our experiment due to a smaller net magnetic moment and a smaller net dynamical stray field.[26] The clear mode profile is also an evidence that antiparallel relative alignment of magnetization state is formed in all the Ni/$Ni_{80}Fe_{20}$ binary structures over the whole array. Thus, we have shown that the dynamic response of the nanostructure is more controllable in the Ni/$Ni_{80}Fe_{20}$ binary structures when compared with the other two structures due to the presence of the two contrasting ferromagnetic materials.

3. Conclusions

We have fabricated high-quality $Ni_{80}Fe_{20}$/$Ni_{80}Fe_{20}$ and Ni/$Ni_{80}Fe_{20}$ binary elliptical nanostructures arranged in three different configurations using a simple self-aligned shadow deposition method. For the control experiment, $Ni_{80}Fe_{20}$ nanostructures were also fabricated from the same resist templates using the conventional electron beam deposition technique. We have also demonstrated that our technique can be applied to other structures, such as binary and thickness modulated nanowires. The static and dynamic properties were investigated using a combination of MOKE and broadband FMR spectroscopy. We showed that the magnetization reversal mechanism can be systematically controlled in the $Ni_{80}Fe_{20}$/$Ni_{80}Fe_{20}$ and Ni/$Ni_{80}Fe_{20}$ binary structures for tailor-made applications. We directly confirmed the magnetization states of the structures at various field histories using magnetic force microscopy. Moreover, our micromagnetic simulations are in very good agreement with the experimental results.

4. Experimental Section

Sample Fabrication: Periodic arrays of ellipsoidal patterns were defined in a 240-nm-thick deep UV resist on top of a 60-nm bottom antireflection coating on silicon substrates by using deep ultraviolet lithography at a wavelength of 248 nm. Three lattice arrangements of the resist template have been fabricated, namely: configuration A ("CNF A") consisting of isolated elements; configuration B ("CNF B") consisting of resist pattern with the elements coupled along the long axis of the ellipse and for configuration C ("CNF C"), the elements of the resist pattern are coupled along the short axis of the ellipse.

The binary nanostructures consisting of one or two ferromagnetic materials were fabricated with a specially designed tilt-table sample holder, using the shadow deposition process and electron beam deposition chamber with a base pressure of 4×10^{-8} Torr. To create Ni/$Ni_{80}Fe_{20}$ binary structures, we performed our depositions with the substrate tilted at ±35° away from the normal direction of the sample. 20-nm-thick Ni and $Ni_{80}Fe_{20}$ films were deposited on the right and left of the pattern with 5-nm-thick Ti capping layer sequentially followed by the lift-off process. For $Ni_{80}Fe_{20}$/$Ni_{80}Fe_{20}$ binary structure, a similar process was used except that the same $Ni_{80}Fe_{20}$ was deposited twice instead of the Ni film.

In order to perform the FMR measurement, coplanar waveguides (CPWs) of signal line width of 20 μm were fabricated on top of the fabricated magnetic structures using conventional optical lithography and metallization of Al_2O_3(50 nm)/Au(150 nm) followed by a lift-off process.

Acknowledgements

This work was supported by the SMF-NUS New Horizon Awards, National Research Foundation, Singapore under Grant No. NRF-G-CRP 2007-05. The authors would like to thank Dr. N. Singh for his help with template fabrication.

Received: May 29, 2012
Revised: August 7, 2012
Published online: October 26, 2012

[1] S. A. Nikitov, P. Tailhades, C. S. Tsai, *J. Magn. Magn. Mater.* **2001**, *236*, 320.
[2] S. Neusser, D. Grundler, *Adv. Mater.* **2009**, *21*, 2927.
[3] K. Lee, S. Kim, *J. Appl. Phys.* **2008**, *104*, 053909.
[4] S. Choi, K.-S. Lee, K. Y. Guslienko, S.-K. Kim, *Phys. Rev. Lett.* **2007**, *98*, 087205.
[5] A. Khitun, M. Bao, K. L. Wang, *J. Phys. D: Appl. Phys.* **2010**, *43*, 264005.
[6] M. Kostylev, P. Schrader, R. L. Stamps, G. Gubbiotti, A. O. Adeyeye, S. Goolaup, N. Singh, *Appl. Phys. Lett.* **2008**, *92*, 132504.
[7] G. Gubbiotti, S. Tacchi, G. Carlotti, P. Vavassory, N. Singh, S. Goolaup, A. O. Adeyeye, A. Stashkevich, M. Kostylev, *Phys. Rev. B* **2005**, *72*, 224413.
[8] A. V. Chumak, A. A. Serga, B. Hillebrands, M. P. Kostylev, *Appl. Phys. Lett.* **2008**, *93*, 022508.
[9] S. Neusser, G. Duerr, H. G. Bauer, S. Tacchi, M. Madami, G. Woltersdorf, G. Gubbiotti, C. H. Back, D. Grundler, *Phys. Rev. Lett.* **2010**, *105*, 067208.
[10] H. Ulrichs, B. Lenk, M. Munzenberg, *Phys. Lett.* **2011**, *97*, 092506.
[11] R. Mandal, S. Saha, D. Kumar, S. Barman, S. Pal, K. Das, A. K. Raychaudhuri, Y. Fukuma, Y. Otani, A. Barman, *ACS Nano* **2012**, *6*, 3397.
[12] Z. K. Wang, V. L. Zhang, H. S. Lim, S. C. Ng, M. H. Kuok, S. Jain, A. O. Adeyeye, *Appl. Phys. Lett.* **2009**, *94*, 083112.
[13] G. Duerr, M. Madami, S. Neusser, S. Tacchi, G. Gubbiotti, G. Carlotti, D. Grundler, *Appl. Phys. Lett.* **2011**, *99*, 202502.
[14] N. Singh, S. Goolaup, A. O. Adeyeye, *Nanotechnology* **2004**, *15*, 1539.
[15] R. P. Hunt, *J. Appl. Phys.* **1967**, *38*, 1652.
[16] J. Brugger, J. W. Berenschot, S. Kuiper, W. Nijdam, B. Otter, M. Elwenspoek, *Microelectron. Eng.* **2000**, *53*, 403.
[17] G. J. Dolan, *Appl. Phys. Lett.* **1977**, *31*, 337.
[18] S. Jain, A. O. Adeyeye, N. Singh, *Nanotechnology* **2010**, *21*, 285702.
[19] D. Bisero, P. Cremon, M. Madami, S. Tacchi, G. Gubbiotti, G. Carlotti, A. O. Adeyeye, *IEEE Trans. Magn.* **2012**, *48*, 1593.
[20] A. Imre, G. Csaba, L. Ji, A. Orlov, G. H. Bernstein, W. Porod, *Science* **2006**, *311*, 205.
[21] M. R. Scheinfein, LLG micromagnetics simulator, *http://llgmicro.home.mindspring.com* (last accessed October 2012).
[22] G. Gubbiotti, S. Tacchi, G. Carlotti, P. Vavassory, N. Singh, S. Goolaup, A. O. Adeyeye, A. Stashkevich, M. Kostylev, *Phys. Rev. B* **2005**, *72*, 224413.
[23] J. Ding, D. Tripathy, A. O. Adeyeye, *Europhys. Lett.* **2012**, *98*, 16004.
[24] J. Ding, S. Jain, A. O. Adeyeye, *J. Appl. Phys.* **2011**, *109*, 07D301.
[25] C. Kittel, *Phys. Rev.* **1948**, *73*, 155.
[26] J. Topp, S. Mendach, D. Heitmann, M. Kostylev, D. Grundler, *Phys. Rev. B* **2011**, *84*, 214413.
[27] J. Ding, M. P. Kostylev, A. O. Adeyeye, *Phys. Rev. B* **2011**, *84*, 054425.
[28] A. A. Awad, G. R. Aranda, D. Dieleman, K. Y. Guslienko, G. N. Kakazei, B. A. Ivanov, F. G. Aliev, *Appl. Phys. Lett.* **2010**, *97*, 132501.